Available online at www.sciencedirect.com
SCIENCE DIRECT®
Journal of Computational Physics 191 (2003) 392–419
JOURNAL OF COMPUTATIONAL PHYSICS
www.elsevier.com/locate/jcp

A robust high-order compact method for large eddy simulation

Santhanam Nagarajan *, Sanjiva K. Lele, Joel H. Ferziger

Department of Mechanical Engineering, Stanford University, Stanford, CA 94305, USA

Received 10 July 2002; received in revised form 11 June 2003; accepted 12 June 2003

Abstract

We present a high-order compact method for large eddy simulation (LES) of compressible turbulent flows. Numerical solution of Navier–Stokes equations with high-order compact methods has been limited by numerical instabilities caused by ill-resolved features of the flow. This problem is alleviated by a staggered arrangement of conserved variables. Simulations of decaying isotropic turbulence at high Reynolds numbers demonstrate the superiority of the present method over the collocated method. Furthermore, the present method is applicable to the conservative form of the governing equations, thereby allowing total energy conservation, a property usually sacrificed in LES with the collocated method. Boundary schemes that extend the present methodology to non-periodic domains are also presented.

Keywords: Large eddy simulation; Compressible turbulent flow; Compact scheme; Staggered grid

1. Introduction

In recent years, large eddy simulation (LES) has been applied to a wide variety of turbulent flows, ranging from problems of scientific interest to those with engineering applications. This development has been possible due to a rapid increase in computational power and a better understanding of the numerical aspects of LES. However, a vast majority of LES research has been devoted to incompressible flows; compressible flow applications have only recently gained attention [1–3].

In LES, unlike other methods, significant energy is present at the high end of the wavenumber spectrum supported by the grid. A numerical scheme for LES should therefore perform well at high wavenumbers. Spectral methods are a natural choice as they are uniformly accurate at all wavenumbers, but have limited application as they impose significant restrictions on geometry and boundary conditions. Furthermore, as a consequence of good resolution at high wavenumbers, aliasing errors are high, and unless explicitly removed, lead to significant degradation of the solution. For successful LES, aliasing errors must be small, and the numerical method should not be overly sensitive to them. Finite difference schemes overcome these restrictions, at the cost of accuracy at high wavenumbers. Complex geometries and boundary conditions

* Corresponding author.
E-mail addresses: snag@stanford.edu (S. Nagarajan), lele@stanford.edu (S.K. Lele), ferziger@stanford.edu (J.H. Ferziger).

0021-9991/$ - see front matter
doi:10.1016/S0021-9991(03)00322-X

are better handled by finite difference or finite element schemes, whose aliasing errors are lower due to damping at high wavenumbers. One such scheme, the second-order finite difference method on a staggered mesh, which has been applied to LES of incompressible flows with remarkable success [4,5], owes its robustness to its ability to conserve kinetic energy, as well as mass and momentum. This property has been extended to higher-order schemes as well [6].

Truncation errors of second-order schemes are large and may exceed the modeled terms in LES [7], making it difficult to differentiate between sources of errors. High-order compact schemes [8] offer a compromise. They perform better than conventional finite difference schemes at high wavenumbers, without the restrictions spectral methods impose on geometry and boundary conditions. These schemes have been successfully applied to direct numerical simulation (DNS) of compressible flows [9–11] and computational aeroacoustics [12], and with limited success to LES [13–15]. The main drawback of these schemes is their sensitivity to aliasing errors which are significantly larger than for explicit finite difference schemes. It has been observed that aliasing is reduced by a modified form of the non-linear advection terms [16–18] and by using a non-conservative form of the energy equation [13,18]. These modifications render this method unsuitable for flows involving shocks because momentum and total energy are not conserved. To apply high-order compact schemes to compressible flows, their robustness needs to be improved without sacrificing conservation. Based on the observations made so far, we can identify four properties required of a numerical method for LES of compressible turbulent flows: (i) high-order accuracy, (ii) good resolution at high wavenumbers, (iii) low sensitivity to aliasing errors, and (iv) conservation of mass, momentum, and total energy.

These conflicting requirements may be reconciled, to some extent, by a staggered arrangement of variables with a high-order compact scheme. The compact scheme provides better resolution at high wavenumbers while staggering of variables, as is demonstrated in this paper, leads to improved robustness. Furthermore, in the staggered case, the governing equations may be cast in the fully conservative form, guaranteeing total energy conservation. Staggered grids have been proposed earlier for solution of the compressible Navier–Stokes equations. Recent research includes that of Kopriva [19] who uses a spectral method along with staggering of flux location with respect to the conserved variables. This allows conservation while using a multi-domain method. Djambazov et al. [20] used a higher-order staggered (in space and time) method to solve the linearized Euler equations for computational aeroacoustics. In their work, Djambazov et al. use staggered location for the variables themselves, but only two of the terms in the equations are treated in a staggered manner. The method presented in this paper involves complete staggering in space, i.e., the conserved variables are located at different points as are the fluxes of each conserved variable. This arrangement leads to a robust method that can be used for LES at high Reynolds numbers.

This paper consists of two parts. In the first part (Sections 2–6), the basic high-order staggered method is analyzed and compared to the collocated method. The governing equations for LES and the sub-grid scale (SGS) models are described in Section 2. The compact finite difference and interpolation schemes are presented in Section 3, and are Fourier analyzed in Section 4. Variable arrangements and discretization of the terms in the governing equations are discussed in Section 5. In Section 6, the superiority of the staggered arrangement is demonstrated through LES of decaying isotropic turbulence. The second part of the paper consists of Sections 7 and 8 wherein boundary schemes for staggered variable arrangement are described and applied to test problems.

2. Governing equations

The governing equations are continuity, momentum, and energy equations in three space dimensions. In Cartesian coordinates (x_1, x_2, x_3) these equations may be written in the following non-dimensional form (dimensional quantities carry a superscript '*')

$$\begin{aligned}
&\frac{\partial \rho}{\partial t} + \frac{\partial}{\partial x_j}(\rho u_j) = 0,\\
&\frac{\partial \rho u_i}{\partial t} + \frac{\partial}{\partial x_j}\left(\rho u_i u_j + p\delta_{ij}\right) = \frac{\partial \sigma_{ij}}{\partial x_j}, \quad i = 1,2,3,\\
&\frac{\partial E}{\partial t} + \frac{\partial}{\partial x_j}\left[(E+p)u_j\right] = -\frac{\partial q_j}{\partial x_j} + \frac{\partial}{\partial x_k}\left(u_j \sigma_{jk}\right),
\end{aligned} \tag{1}$$

where ρ, u_i, p, E, σ_{ij}, and q_i are the density, velocity vector, pressure, total energy, viscous stress tensor, and heat flux vector, respectively

$$E = \frac{p}{\gamma - 1} + \frac{1}{2}\rho u_k u_k, \tag{2}$$

$$\sigma_{ij} = \frac{\mu}{Re}\left(\frac{\partial u_i}{\partial x_j} + \frac{\partial u_j}{\partial x_i} - \frac{2}{3}\frac{\partial u_k}{\partial x_k}\delta_{ij}\right), \tag{3}$$

$$q_i = -\frac{\mu}{Re\,Pr}\frac{\partial T}{\partial x_i}, \tag{4}$$

where $Re = \rho_0^* c_0^* L_0^*/\mu_0^*$ is a Reynolds number based on the reference density ρ_0^*, velocity c_0^* (the reference sound speed), length scale L_0^*, and coefficient of viscosity μ_0^* at the reference conditions. $Pr = \mu_0^* C_p^*/k^*$ is the Prandtl number. The above set is closed by the equation of state

$$p = \frac{\gamma - 1}{\gamma}\rho T.$$

The set (1) of equations may be written in vector form as

$$\frac{\partial U}{\partial t} + \frac{\partial F_i}{\partial x_i} = 0, \tag{5}$$

where

$$U = \begin{pmatrix} \rho \\ \rho u_1 \\ \rho u_2 \\ \rho u_3 \\ E \end{pmatrix}, \quad F_i = \begin{pmatrix} \rho u_i \\ \rho u_1 u_i + p\delta_{i1} - \sigma_{i1} \\ \rho u_2 u_i + p\delta_{i2} - \sigma_{i2} \\ \rho u_3 u_i + p\delta_{i3} - \sigma_{i3} \\ (E+p)u_i + q_i - u_k \sigma_{ik} \end{pmatrix}, \tag{6}$$

where U is the vector of conserved variables and F_i is the flux vector in the x_i-direction.

To obtain the LES equations, a filter is needed. The kernel of a spatial filter over a domain Ω is denoted by $G(\mathbf{x})$ and a filtered quantity (denoted by an overbar) is defined as

$$\bar{f}(x) = \int_\Omega G(\mathbf{x} - \mathbf{x}') f(\mathbf{x}')\,\mathrm{d}\mathbf{x}'. \tag{7}$$

The compressible LES equations are simpler if Favre (density-weighted) filtering (denoted by a "~") defined as

$$\tilde{f} = \frac{\overline{\rho f}}{\bar{\rho}} \tag{8}$$

is utilized. The equations for LES are derived using the filter (7) on the governing equations (1) (see [13] for details). Assuming that filtering commutes with differentiation, we get

$$\begin{aligned}
&\frac{\partial \overline{\rho}}{\partial t} + \frac{\partial}{\partial x_j}\left(\overline{\rho}\widetilde{u}_j\right) = 0,\\
&\frac{\partial \overline{\rho}\widetilde{u}_i}{\partial t} + \frac{\partial}{\partial x_j}\left(\overline{\rho}\widetilde{u}_i\widetilde{u}_j + \overline{p}\delta_{ij}\right) = \frac{\partial \overline{\sigma}_{ij}}{\partial x_j} - \frac{\partial \tau_{ij}^{\mathrm{sgs}}}{\partial x_j},\\
&\frac{\partial \overline{E}}{\partial t} + \frac{\partial}{\partial x_j}\left[\left(\overline{E}+\overline{p}\right)\widetilde{u}_j\right] = -\frac{\partial \overline{q}_j}{\partial x_j} + \frac{\partial}{\partial x_k}\left(\widetilde{u}_j\overline{\sigma}_{jk}\right) - \frac{\partial q_j^{\mathrm{sgs}}}{\partial x_j},
\end{aligned} \tag{9}$$

where $\overline{\sigma}_{ij}$ and $\overline{q}_i$ are the filtered stress tensor and heat flux, respectively. These terms, along with the sub-grid terms τ_{ij}^{sgs} and q_j^{sgs} are described in Appendix A.

3. Numerical schemes

In this section, we present high-order compact schemes for collocated and staggered grids used in this paper (see [8] for a more general and complete discussion of such schemes). In each case, a one-parameter family of fourth-order schemes is presented. The schemes we use are the single sixth-order scheme that each family yields for a particular value of the free parameter.

To define the finite difference schemes and to Fourier analyze them, we consider 1-D collocated and staggered grids. Considering a uniformly spaced grid, as shown in Fig. 1, with nodes at $x_j = (j-1)\Delta x$ for $0 \leqslant j \leqslant N$ (where Δx is the grid spacing) a *collocated scheme* evaluates the derivative of f at these nodes using the function values $f_j = f(x_j)$ whereas a *staggered scheme* uses function values located half a cell width away, i.e., at nodes with indices $\{1/2, \ldots, j-1/2, j+1/2, \ldots, N-1/2\}$.

3.1. Approximation of first derivative

A high-order compact finite difference approximation for the first derivative $f' = \mathrm{d}f/\mathrm{d}x$ at the nodes $j = 0, \ldots, N$ is given by

$$\hat{\alpha} f'_{j-1} + f'_j + \hat{\alpha} f'_{j+1} = b\frac{f_{j+2} - f_{j-2}}{4\Delta x} + a\frac{f_{j+1} - f_{j-1}}{2\Delta x}. \tag{10}$$

Matching coefficients of the Taylor series expansion gives relationships among the parameters $\hat{\alpha}$, a and b. Doing so to fourth order yields a one-parameter family of fourth-order schemes with

$$a = \tfrac{2}{3}(2 + \hat{\alpha}), \tag{11}$$

$$b = \tfrac{1}{3}(-1 + 4\hat{\alpha}). \tag{12}$$

The leading order truncation error vanishes for $\hat{\alpha} = 1/3$ resulting in a sixth-order compact scheme which we call *the basic collocated difference scheme*.

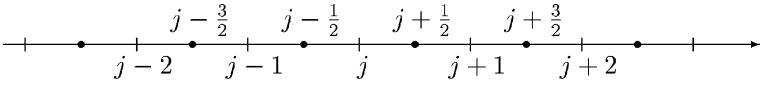

Fig. 1. 1-D grid for collocated and staggered schemes.

If the function values are available half a grid spacing from the nodes, i.e., $f_{j+1/2} = f(x_{j+1/2})$ are given, a high-order compact scheme for evaluating the derivative f'_j at the node x_j is

$$\hat{\alpha} f'_{j-1} + f'_j + \hat{\alpha} f'_{j+1} = b\frac{f_{j+3/2} - f_{j-3/2}}{3\Delta x} + a\frac{f_{j+1/2} - f_{j-1/2}}{\Delta x}. \tag{13}$$

Once again, this is a family of fourth-order schemes if

$$a = \tfrac{3}{8}(3 - 2\hat{\alpha}), \tag{14}$$

$$b = \tfrac{1}{8}(-1 + 22\hat{\alpha}). \tag{15}$$

The *basic staggered difference scheme* of sixth order is obtained for $\hat{\alpha} = 9/62$.

3.2. Approximation of second derivative

Evaluation of viscous terms requires second derivatives on collocated meshes but not in the case of the staggered arrangement (see Section 5). A compact scheme for the second derivative f''_j is

$$\hat{\alpha} f''_{j-1} + f''_j + \hat{\alpha} f''_{j+1} = b\frac{f_{j+2} - 2f_j + f_{j-2}}{4\Delta x^2} + a\frac{f_{j+1} - 2f_j + f_{j-1}}{2\Delta x^2}. \tag{16}$$

For fourth-order accuracy, the following relations need to be satisfied:

$$a = \tfrac{4}{3}(1 - \hat{\alpha}), \tag{17}$$

$$b = \tfrac{1}{3}(-1 + 10\hat{\alpha}). \tag{18}$$

A single sixth-order scheme is obtained when $\hat{\alpha} = 2/11$.

3.3. Interpolation scheme

The staggered method involves midpoint interpolation, which is carried out by an approximation of the form

$$\hat{\alpha} f^{\mathrm{I}}_{j-1} + f^{\mathrm{I}}_j + \hat{\alpha} f^{\mathrm{I}}_{j+1} = \frac{b}{2}\left(f_{j+3/2} + f_{j-3/2}\right) + \frac{a}{2}\left(f_{j+1/2} + f_{j-1/2}\right), \tag{19}$$

where f^{I}s are the interpolated values. For fourth-order accuracy, the coefficients are related by

$$a = \tfrac{1}{8}(9 + 10\hat{\alpha}), \tag{20}$$

$$b = \tfrac{1}{8}(6\hat{\alpha} - 1), \tag{21}$$

with $\hat{\alpha} = 3/10$ yielding a sixth-order scheme.

Of the four properties outlined in Section 1, schemes described so far satisfy the high-order accuracy requirement. In the following section, the second property, viz. good resolution characteristics, is demonstrated by Fourier analysis.

4. Fourier analysis of errors

Fourier analysis allows us to quantify errors at resolved wavenumbers and demonstrates the suitability of a scheme for LES wherein it is necessary to represent all wavenumbers accurately. For Fourier analysis, we consider a function $f(x)$ that is periodic over the domain $[0, L]$. For an equally spaced grid with $N+1$ nodes, $\Delta x = L/N$, and the Fourier representation of f is

$$f(x) = \sum_{k=-N/2}^{N/2-1} \hat{f}_k \exp\left(\frac{2\pi \mathrm{i} k x}{L}\right), \tag{22}$$

where $\mathrm{i} = \sqrt{-1}$. Introducing the scaled wavenumber $\omega = 2\pi k \Delta x/L = 2\pi k/N$ and the scaled coordinate $s = x/\Delta x$ simplifies the Fourier modes to $\mathrm{e}^{\mathrm{i}\omega s}$, where $\omega \in [-\pi, \pi]$. Differentiating the scaled representation $f(s)$ with respect to s yields

$$f'(s) = \sum_{k=-N/2}^{N/2-1} \mathrm{i}\omega \hat{f}_k \exp(\mathrm{i}\omega s). \tag{23}$$

Therefore $\hat{f}' = \mathrm{i}\omega \hat{f}$. Differencing errors may be assessed by comparing the Fourier coefficients of the first derivative obtained using the finite difference scheme $(\hat{f}'_k)_{\mathrm{fd}} = \mathrm{i}\omega' \hat{f}_k$ to those of the exact derivative $\hat{f}'_k = \mathrm{i}\omega \hat{f}_k$, i.e., comparing ω' and ω. Exact differentiation therefore corresponds to $\omega' = \omega$, a relation spectral methods reproduce faithfully (except at $\omega = \pi$). The functional dependence of ω' on ω for staggered differentiation is obtained by setting $f(s) = \mathrm{e}^{\mathrm{i}\omega s}$ in (13) as

$$\omega'(\omega) = \frac{2a \sin(\omega) + \frac{2}{3} b \sin(3\omega/2)}{1 + 2\hat{\alpha} \cos(\omega)}. \tag{24}$$

Similar expressions may be obtained for the other derivative schemes. In Fig. 2, the modified wavenumber ω' is depicted as a function of ω for various schemes. It is apparent that staggered schemes approximate the exact wavenumber better than collocated schemes. In fact, even for second-order central differences, representation of high wavenumbers by the staggered scheme is markedly superior to that of the collocated scheme. Furthermore, representation of high wavenumbers improves significantly with order of accuracy. It is clear that staggered differentiation, along with high-order accuracy, provides better resolution at high wavenumbers.

A Fourier analysis of second derivative schemes that are needed to evaluate the viscous terms sheds light on the accuracy of these terms at high wavenumbers. These terms are of the form

$$\frac{\partial}{\partial x}\left(\mu \frac{\partial u}{\partial x}\right) = \frac{\partial \mu}{\partial x}\frac{\partial u}{\partial x} + \mu \frac{\partial^2 u}{\partial x^2}. \tag{25}$$

Either side of the above equality may be used to evaluate the viscous terms. The LHS of (25), which is in the conservative form, involves two applications of the first derivative scheme while the RHS, a non-conservative form, involves a second derivative evaluation. The modified wavenumber (assuming μ is uniform in space) obtained from Fourier analysis of these methods are shown in Fig. 3. On collocated meshes, the conservative form provides very poor representation at high wavenumbers whereas the non-conservative form does much better, and is therefore preferred. On the other hand, on a staggered mesh, the conservative form (which evaluates the viscous term at the same location as the function f) may be used as it causes little degradation of high-wavenumber components. Furthermore, better resolution provided by the high-order compact method compared to second-order central difference is also evident.

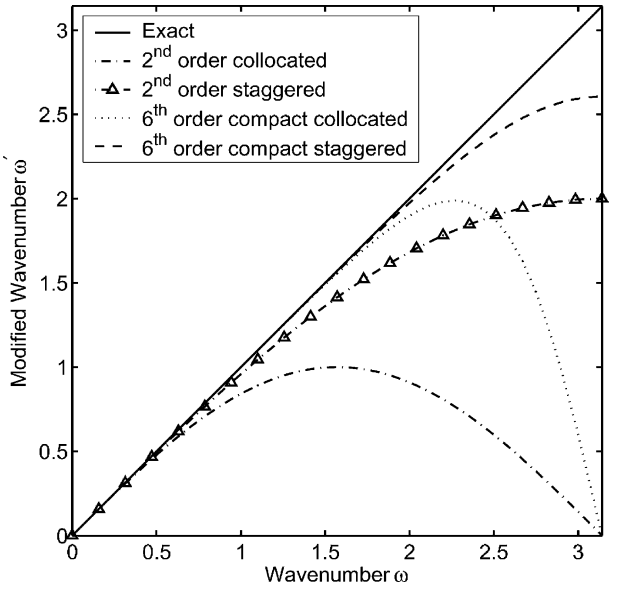

Fig. 2. Modified wavenumber spectrum of various first derivative operators.

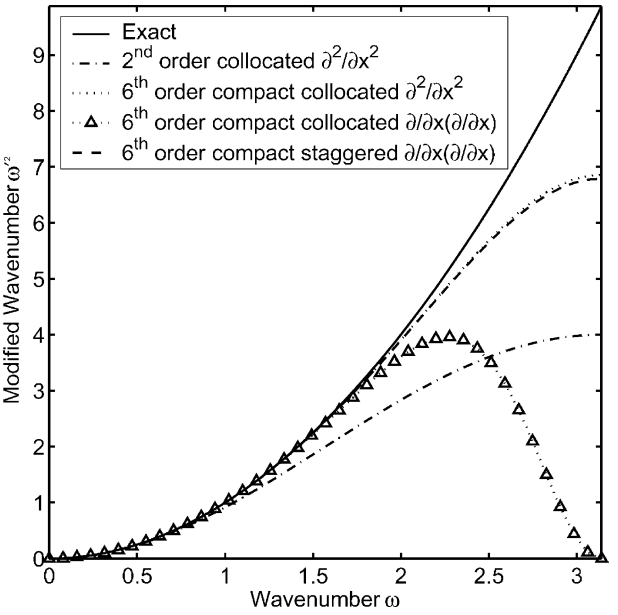

Fig. 3. Modified wavenumber spectrum of various second derivative operators. Curves for the collocated scheme (dotted line) and two first derivative evaluations with the staggered scheme (dashed line) lie almost on each other.

Fourier coefficients of the interpolated function are compared to those of the original function to assess the resolving power of the interpolation scheme. Ideally, the coefficients should remain unchanged after interpolation. The accuracy of an interpolation scheme and its resolution properties are characterized by a

transfer function that is the ratio of the Fourier coefficient (at each wavenumber) of the interpolated function to that of the original function. This ratio is obtained by setting $f(s) = e^{i\omega s}$ in (19),

$$T(\omega) = \frac{a\cos(\omega/2) + b\cos(3\omega/2)}{1 + 2\hat{\alpha}\cos(\omega)}. \tag{26}$$

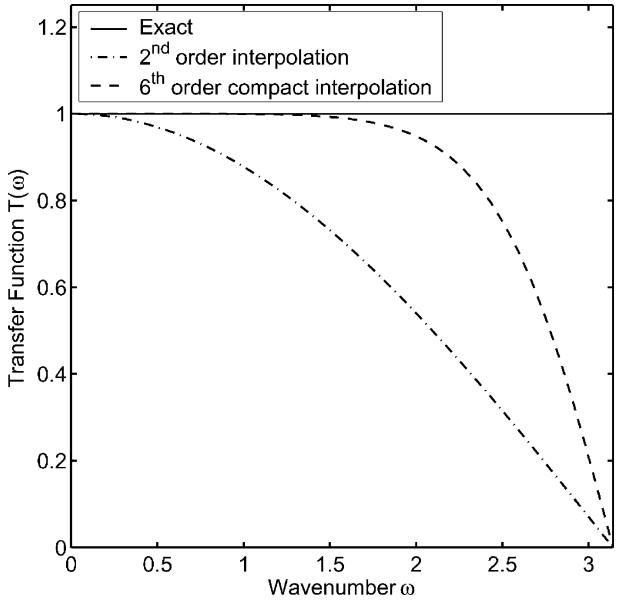

Fig. 4. Transfer function of interpolation operators.

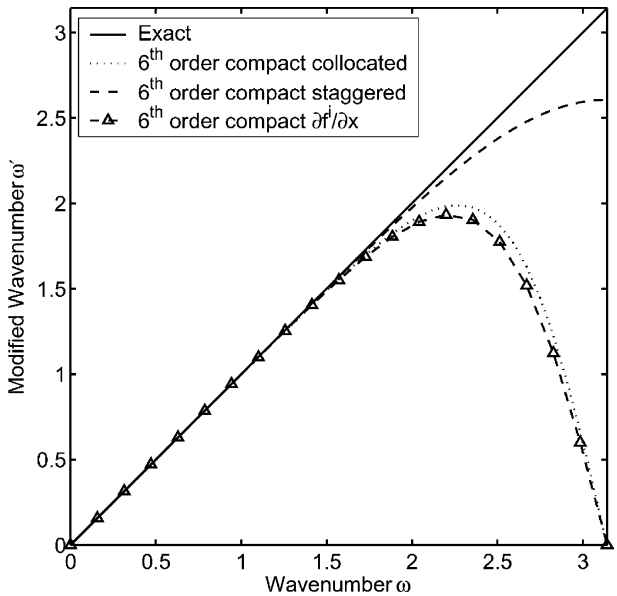

Fig. 5. Modified wavenumber spectrum of interpolation + staggered derivative operator compared to collocated and staggered differences.

Transfer functions for the second-order explicit and sixth-order compact interpolation are shown in Fig. 4. The compact scheme resolves high-wavenumbers with greater accuracy.

In the staggered arrangement (to be discussed in the following section), derivatives of advective fluxes are obtained by application of the staggered compact scheme to an interpolated function. This leads to damping of high wavenumbers. The modified wavenumber of this composite operation is the product of the modified wavenumbers of staggered differencing and the transfer function of interpolation. This is depicted in Fig. 5 (triangles), and is clearly very close to that of the compact scheme on a collocated mesh. Thus, staggering does not affect the resolution characteristics of the non-linear terms in the governing equations.

We conclude this section by observing that, in all cases, compact schemes provide better resolution than central difference schemes at high-wavenumber. Furthermore, staggering either improves upon or causes very little change in resolution characteristics of collocated grids. Therefore, high-order compact schemes satisfy two of the requirements stated at the outset, viz. (i) high order of accuracy and (ii) better resolution at high wavenumbers. In the following section, we discuss the arrangement of variables for the Navier–Stokes equations and the choice of schemes for each arrangement. The third property, robustness brought about by reduced sensitivity to aliasing errors, is also discussed.

5. Variable arrangement and discretization of the governing equations

In this section, two kinds of variable arrangements are discussed and the method used to update the governing equations is outlined for each case.

5.1. Collocated arrangement

In the collocated arrangement (shown in Fig. 6(a)), all dependent variables are located at the same point. This arrangement is widely used for compressible flow calculations and LES of turbulent flows have been conducted on such meshes with sixth-order compact schemes [13–15]. However, these researchers found that certain modifications to the governing equations improve robustness. First, the non-linear advection terms are recast in a modified form (see [16] for further details):

$$\frac{\partial}{\partial x_j}\left(\overline{\rho}\widetilde{u}_i\widetilde{u}_j\right) = \frac{1}{2}\frac{\partial}{\partial x_j}\left(\overline{\rho}\widetilde{u}_i\widetilde{u}_j\right) + \frac{1}{2}\overline{\rho}\widetilde{u}_i\frac{\partial \widetilde{u}_j}{\partial x_j} + \frac{1}{2}\widetilde{u}_j\frac{\partial}{\partial x_j}\left(\overline{\rho}\widetilde{u}_i\right). \tag{27}$$

This leads to reduction of aliasing errors. It has been observed that employing the equation for internal energy instead of the total energy equation also improves the robustness of LES calculations. In place of the energy equation in (1), the following is used

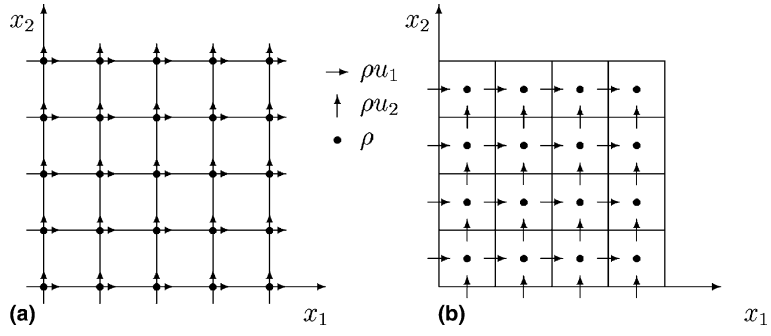

Fig. 6. Arrangement of variables in two dimensions: (a) collocated and (b) staggered.

$$\frac{\partial}{\partial t}(\overline{\rho}\widetilde{T}) + \frac{\partial}{\partial x_j}(\overline{\rho}\widetilde{u}_j\widetilde{T}) + \gamma\overline{p}\frac{\partial \widetilde{u}_j}{\partial x_j} = \gamma\widetilde{\sigma}_{ij}\frac{\partial \widetilde{u}_i}{\partial x_j} + \gamma\frac{\partial}{\partial x_j}\left(\frac{\widetilde{\mu}}{RePr}\frac{\partial \widetilde{T}}{\partial x_j}\right) - \frac{\partial q_j^{\mathrm{sgs}}}{\partial x_j}. \tag{28}$$

Since internal energy is not a conserved quantity, energy conservation is not guaranteed when (28) is used, rendering the collocated method unsuitable for compressible flows that involve shocks. Note also that the convective terms in the energy equation may also be recast in the modified form to reduce aliasing errors.

The discretization scheme used for the convective and pressure terms in the governing equations is the sixth-order collocated first derivative scheme. For the viscous terms in the momentum equation, two applications of the first derivative operator reduces in magnitude the high wavenumber components (as shown in Fig. 3) of the viscous terms. This translates to insufficient resolution of viscous terms at high wavenumbers and is undesirable. These terms are therefore recast in the non-conservative form using the chain rule and the second derivative operation with the sixth-order collocated scheme is used.

5.2. Staggered arrangement

The staggered arrangement of variables is shown in Fig. 6(b). Such an arrangement was first proposed in [21] to overcome the problem of pressure–velocity decoupling in incompressible flows. In this arrangement, momenta are located half a cell width from thermodynamic variables. Fig. 7 shows the location of the conserved variables and fluxes for update of the continuity and x_1-momentum equations. For the continuity equation, the fluxes ρu_1 and ρu_2 are located naturally at the cell faces whereas, for the x_1-momentum equation, all fluxes except the advective ones are located at the cell faces. The advection terms $\rho u_1 u_1$ and $\rho u_1 u_2$ need to be evaluated at the cell faces by interpolation. Once the fluxes are available at the locations shown in Fig. 7, the staggered derivative scheme is used to evaluate the flux derivatives at the variable location. It should be noted that there are many ways in which some of the terms can be evaluated in the staggered method. The method chosen was arrived at by trying out the various options available and then choosing the most robust one. For example, advection terms (e.g., $\rho u_1 u_2$ in the x-momentum equation) need to be interpolated. This was done by interpolating the mass flux (ρu_2) and the velocity (u_2) to the node shown by an open circle in Fig. 7, multiplying the two, and differentiating using the staggered scheme. The viscous stress tensor, on the other hand, is naturally located (as shown in Fig. 7) and requires no interpolation. A similar methodology is followed for advective and heat-flux terms in the energy equation. The terms $\partial(u_i\sigma_{ij})/\partial x_j$ use three interpolations (when $i \neq j$) to shift u_i and σ_{ij} to the u_j-node. The interpolated values are then multiplied and differentiated to get their contribution to the energy equation.

In this section, the problems associated with the use of high-order compact schemes with the collocated arrangement have been described. The staggered arrangement has also been discussed, but the advantages of staggering are not yet evident. The superiority of the staggered arrangement is revealed through LES of isotropic turbulence, presented in the following section.

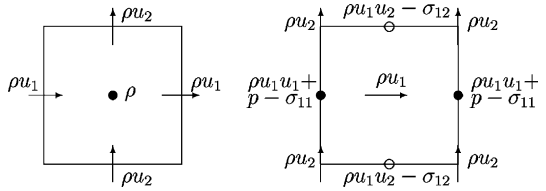

Fig. 7. Variable and flux location on a staggered grid: (a) continuity equation and (b) x_1-momentum equation.

6. Numerical experiments

In this section, the staggered method is validated against experiments and compared to the following collocated methods:

- *Collocated method I* uses the fully conservative form of the total energy equation along with the modified form of the convective and non-conservative form of the viscous and heat flux terms.
- *Collocated method II* uses the internal energy equation and the modified form of the convective terms in both the momentum and energy equations along with the non-conservative form of the viscous and heat flux terms.

A third-order Runge–Kutta scheme is used for time marching, with the Courant number limited to small values (<0.1) to minimize errors associated with time integration.

Temporal decay of homogeneous isotropic turbulence is chosen as the test problem as it avoids complications arising from boundary conditions while providing an accurate assessment of the suitability of a scheme for LES. The characteristic scales of decaying isotropic turbulence are the rms velocity fluctuation u^*_{rms} and the Taylor microscale λ^* which yield the time scale $\tau^*_t = \lambda^*/u^*_{\mathrm{rms}}$. The characteristic non-dimensional parameters are the microscale Reynolds number and turbulent Mach number defined by

$$Re_\lambda = \frac{u^*_{\mathrm{rms}}\lambda^*}{v^*}, \tag{29}$$

$$M_{\mathrm{t}} = \frac{q^*}{c^*_0} = \frac{\sqrt{3}u^*_{\mathrm{rms}}}{c^*_0}, \tag{30}$$

where v^* is the kinematic viscosity, c^*_0 is the speed of sound of the mean state, and $q^{*^2} = 3\,u^{*^2}_{\mathrm{rms}}$.

6.1. Validation of staggered method – comparison with experiments

The staggered method and its implementation are validated against the benchmark experiments of grid-generated turbulence by Comte-Bellot and Corrsin [22]. The simulation is carried out on a 32^3 grid with an initial velocity field that is solenoidal, has an energy spectrum measured at one of the stations in the experiment, and random phase relationship between the modes. The initial Taylor microscale Reynolds number, associated with the measurement location in the experiment, is 71.6. The temporal development of turbulence in the simulation is then compared to the spatial development observed in [22] after relating the two through Taylor's hypothesis. It should be noted that the experiments were conducted in the incompressible regime whereas the simulations performed here are compressible. For an initial turbulent Mach number of $M_{\mathrm{t}} = 0.3$, the differences are not expected to be large. In Figs. 8 and 9 the results from the numerical simulation are compared to those from the experiment. Fig. 8 shows the decay of turbulent kinetic energy as a function of time and Fig. 9 depicts the energy spectrum at a later time (downstream location in the experiment). The good agreement between computed and experimental results provides a validation of the staggered method.

6.2. Test of robustness – high Re simulations

A method for LES is considered robust if it is able to handle high *Re* simulations with relatively few grid points, i.e., it supports under-resolved simulations. Two studies that demonstrate robustness of the staggered method are presented: the first compares the performance of the staggered method and collocated method I that employs the total energy equation, while the second compares the staggered method and collocated method II. All simulations have been carried out on a 32^3 grid, with an initial energy spectrum

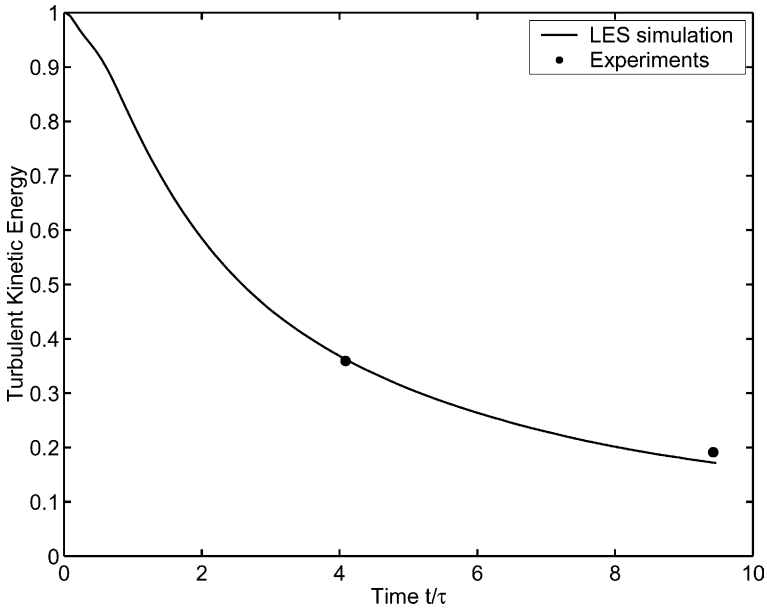

Fig. 8. Validation of staggered method – comparison of simulated decay of turbulent kinetic energy with the experiment of Comte-Bellot and Corrsin [22].

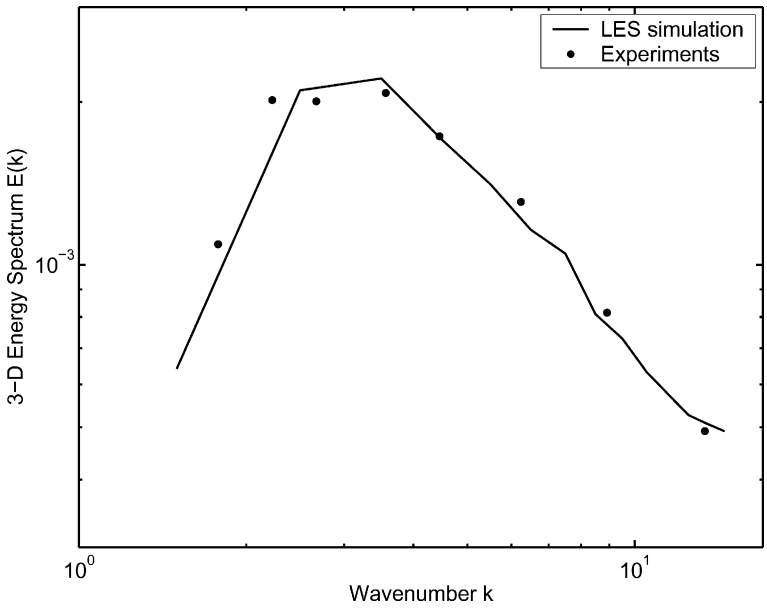

Fig. 9. Validation of staggered method – comparison of calculated energy spectrum with the experiment of Comte-Bellot and Corrsin [22].

$$E(k) = 16\sqrt{\frac{2}{\pi}}\frac{u_{\mathrm{rms}}^2}{k_0}\left(\frac{k}{k_0}\right)^4 \exp\left[-2\left(\frac{k}{k_0}\right)^2\right]. \tag{31}$$

Initial velocity fields are solenoidal and initial thermodynamic fields are uniform in space. This corresponds to the initial condition IC4 in [23] which they find to be the most severe in terms of dilatation developed in the transient.

For the first comparison, simulations are carried out at a turbulent Mach number of $M_t = 0.3$ and three Reynolds numbers, $Re_\lambda = 100$, 500, and 1000. The most energetic scales in the initial spectrum occur at $k_0 = 4$. The staggered method and collocated method I are run at these conditions and the results are compared. Fig. 10 shows the decay of turbulent kinetic energy predicted by the two methods at various Reynolds numbers. At $Re = 100$ the decay predicted by the staggered method and collocated method I are in good agreement. At higher Reynolds numbers (500 and 1000), the agreement between the two methods is still very good, but the collocated method fails after some time. Failure of the collocated method occurs due to growth of rms fluctuations of thermodynamic variables, as illustrated in Fig. 11, which shows the evolution of rms density fluctuations predicted by collocated method I in the three simulations. At high Reynolds numbers, density fluctuations increase in an unbounded manner, causing instability. On the other hand, the staggered grid solution behaves well even at high Reynolds numbers, as shown by the rms density fluctuation history in Fig. 12. It should be noted that for a given initial field, as Re increases, viscous terms become negligible and sub-grid terms are responsible for energy dissipation. In the limit, the simulations should become independent of Re as the sub-grid model does not depend on Re (see Appendix A). This trend is captured by the staggered method, as evident from Figs. 10 and 12 wherein the difference between $Re_\lambda = 500$ and 1000 curves is much smaller than that between $Re_\lambda = 100$ and 500 curves. It should also be noted that as Re increases, behavior of the solution is dictated completely by the interaction of the numerical method and the sub-grid model. If the numerical method remains stable in the presence of large errors, the sub-grid model will eventually drain energy from the high wavenumber before instabilities occur.

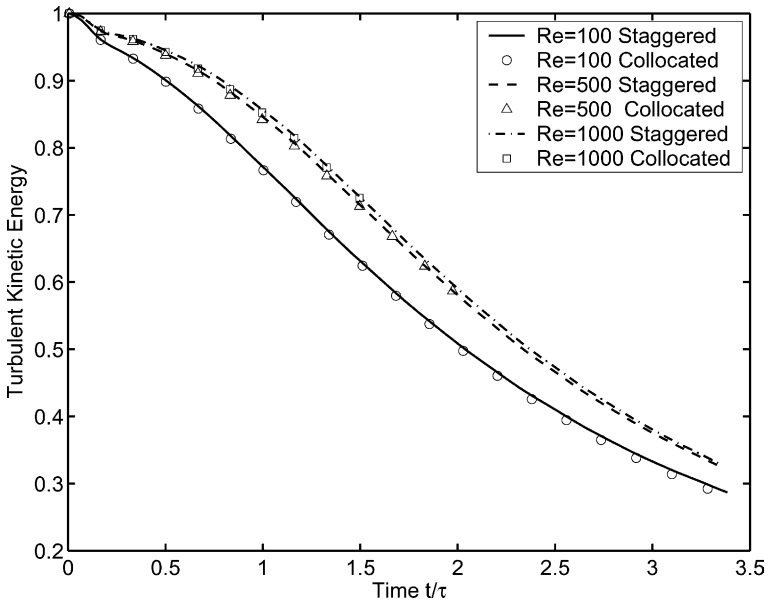

Fig. 10. Comparison of staggered method with method I – decay of turbulent kinetic energy at different Reynolds numbers.

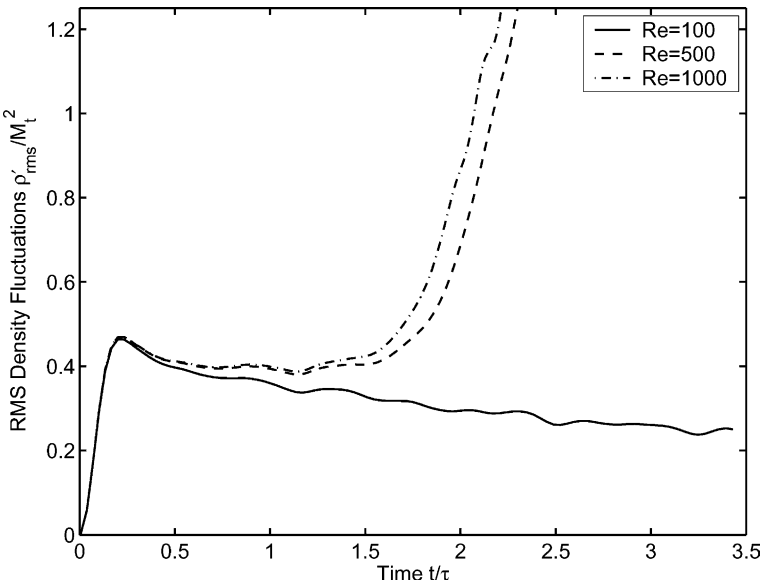

Fig. 11. Method I – evolution of rms density fluctuations.

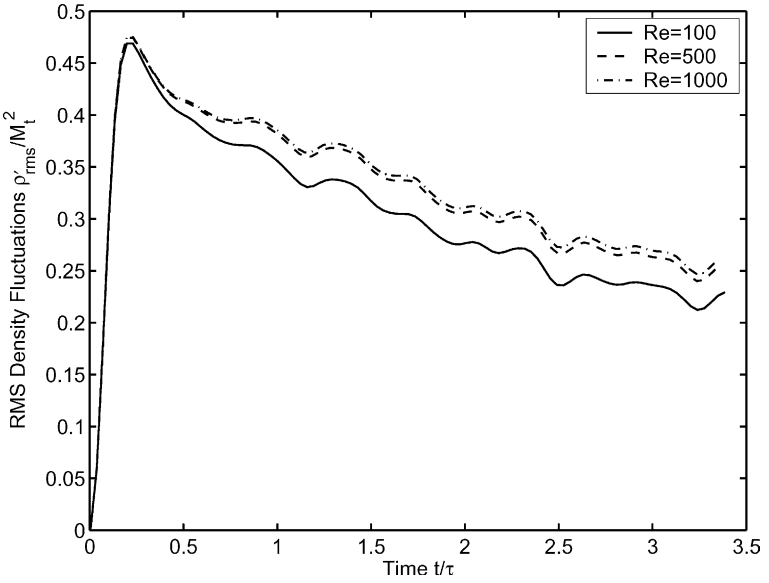

Fig. 12. Staggered method – evolution of rms density fluctuations at the same conditions as Fig. 11.

The staggered method shows this behavior whereas the collocated method does not. Furthermore, as Reynolds number increases, the shift of the kinetic energy decay curve follows the trends observed in the direct numerical simulations of Samtaney et al. [23]. In the absence of a sub-grid model, i.e., an under-resolved direct numerical simulation (DNS), the present scheme causes a transfer of energy from the internal to the kinetic mode. As a result, LES without a sub-grid model is not stable at Reynolds numbers larger than $Re_\lambda \sim 300$ on a 32^3 grid; failure occurs at $t/\tau \sim 3$ for $Re_\lambda \sim 400$.

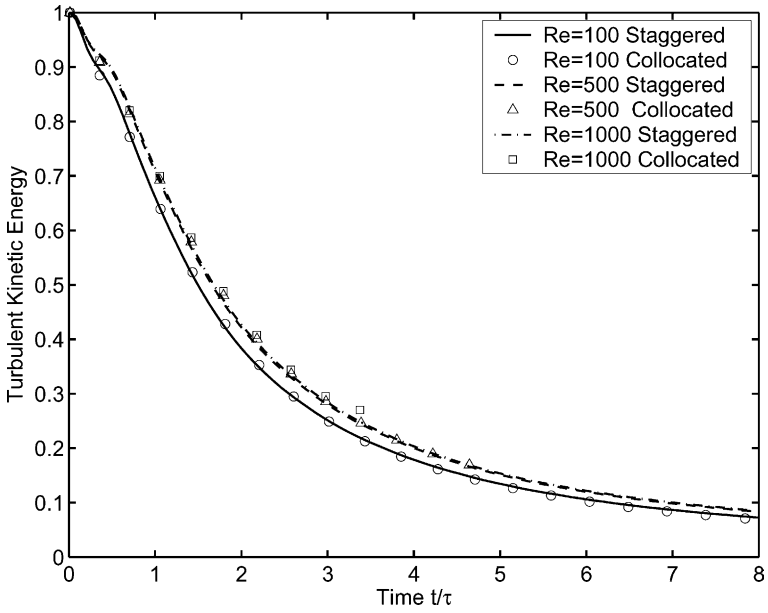

Fig. 13. Comparison of staggered method with method II – decay of turbulent kinetic energy at different Reynolds numbers.

The staggered method is now compared to collocated method II that uses the internal energy equation. As mentioned earlier, use of the internal energy equation improves robustness of the collocated method. As a result, higher Reynolds numbers can be attained. To bring out the differences between the two schemes, this comparison is carried out at conditions more stringent than the earlier case. The turbulent Mach number is raised (to $M_t = 0.4$) as is the location of the peak in the initial spectrum (to $k_0 = 7$). Once again the Reynolds numbers for the three simulations are taken to be $Re_\lambda = 100$, 500, and 1000. Under these conditions, collocated method I fails even at $Re_\lambda = 100$. The decay of turbulent kinetic energy is shown in Fig. 13. Once again, in terms of kinetic energy, the collocated method compares well with the staggered method at all Reynolds numbers. However, the collocated method simulations at higher Reynolds numbers fail due to and unbounded increase of thermodynamic fluctuations. This is clear from Fig. 14 which shows as sudden increase in the density fluctuations for high Reynolds numbers. On the other hand, the staggered method behaves well at high Reynolds numbers, as is clear from Fig. 15.

Figs. 13 and 14 show that turbulent kinetic energy is well behaved while fluctuations in thermodynamic quantities are not. Thus, we may conclude that instabilities arise from the energy equation. This is confirmed by the oscillatory behavior of turbulent Prandtl number in the collocated case as shown in Fig. 16. There are oscillations in Prandtl number in the staggered case as well, but these are confined to the initial transient and do not lead to catastrophic failure as in the collocated case. One is led to conclude that these instabilities are due to interaction of the scheme with the sub-grid model. Furthermore, collocated method II uses the internal energy equation. As a result, total energy is not expected to be conserved by this method, as evident from Fig. 17 depicting the time evolution of total energy in the domain. The staggered scheme which uses the total energy equation conserves it, whereas, at all Reynolds numbers, collocated method II suffers from a decrease in total energy by as much as 3%. This is undesirable when dealing with shocks and heating/cooling. In these simulations, Mach number reaches locally supersonic values and eddy-shocklets are present.

The simulations just described use initial conditions ($M_t = 0.4$, $k_0 = 7$ and $Re_\lambda = 100$, 500, and 1000) that are very similar to one case in [23] (case $D8$ with $M_t = 0.5$, $k_0 = 8$, and $Re_\lambda = 72$ with no variations in the

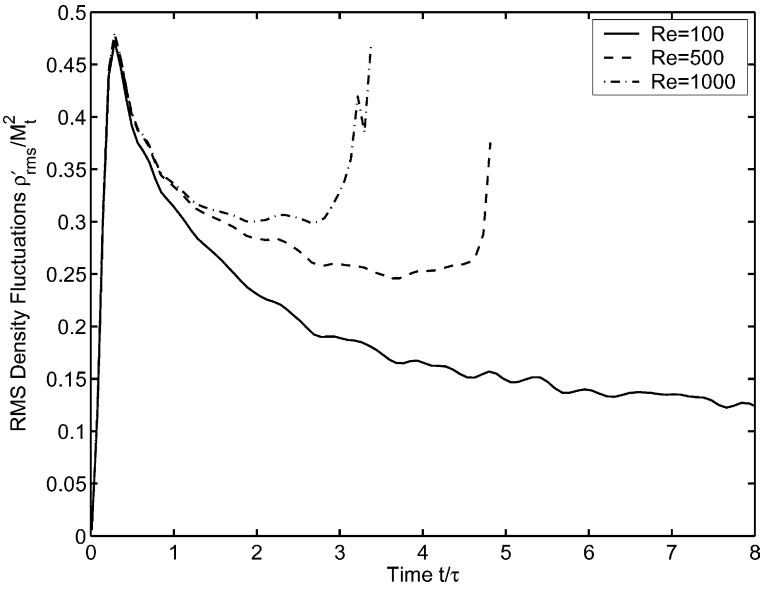

Fig. 14. Method II – evolution of rms density fluctuations at three Reynolds numbers.

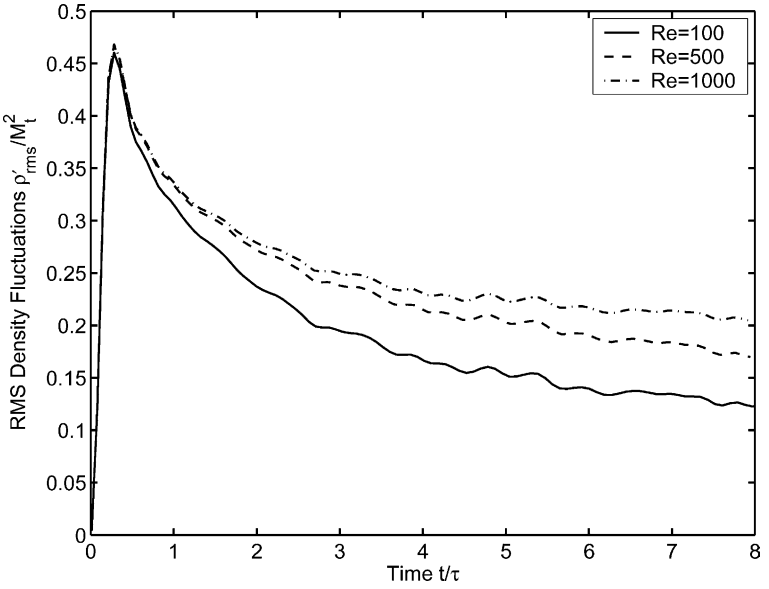

Fig. 15. Staggered method – evolution of rms density fluctuations at the same conditions as Fig. 14.

initial thermodynamic field). A comparison of rms density history obtained using the the staggered method with [23] is shown in Fig. 18. The 64^3 LES result (solid line) at conditions corresponding to case *D*8 of Samtaney et al. [23] shows good agreement with their DNS (symbols from Fig. 5 in [23] are unfiltered values). A slight underprediction of rms density by the LES, as evident in Fig. 18, is to be expected as the DNS results are unfiltered and therefore contain scales that the LES does not resolve. Another comparison,

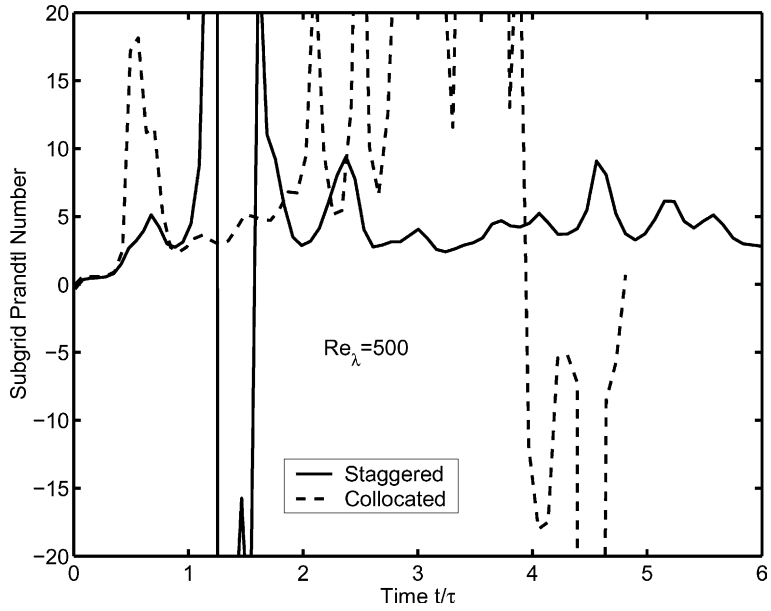

Fig. 16. Comparison of staggered method with method II – time history of turbulent Prandtl number.

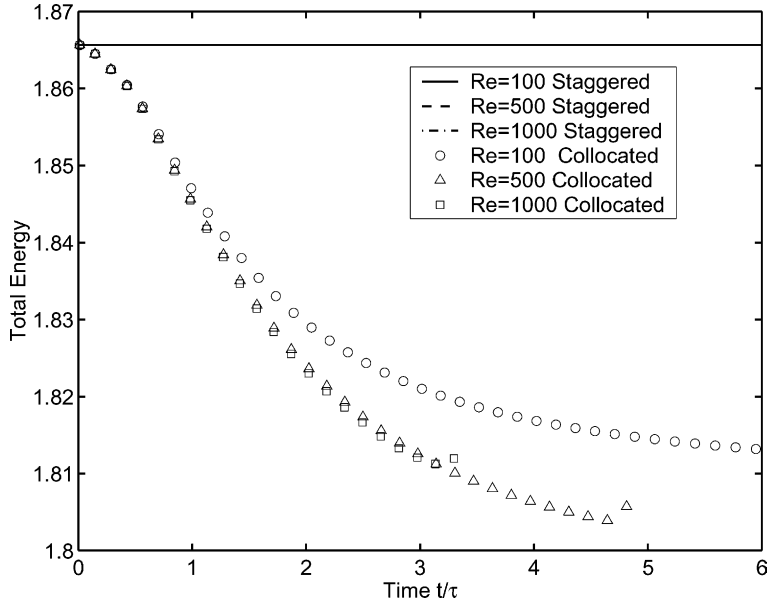

Fig. 17. Comparison of staggered method with method II – conservation of total energy in the domain. The lines corresponding to the staggered method are indistinguishable.

this of the probability density function of Mach number, is made in Fig. 19 between case $D9$ of Samtaney et al. (see Fig. 18 in [23]) and a 64^3 LES conducted at the same conditions ($M_t = 0.488$, $k_0 = 4$, and $Re_\lambda = 175$). The Mach number PDF calculated at $t/\tau = 1.95$ ($= 1.56$ based on the definition of τ used in [23]) agrees

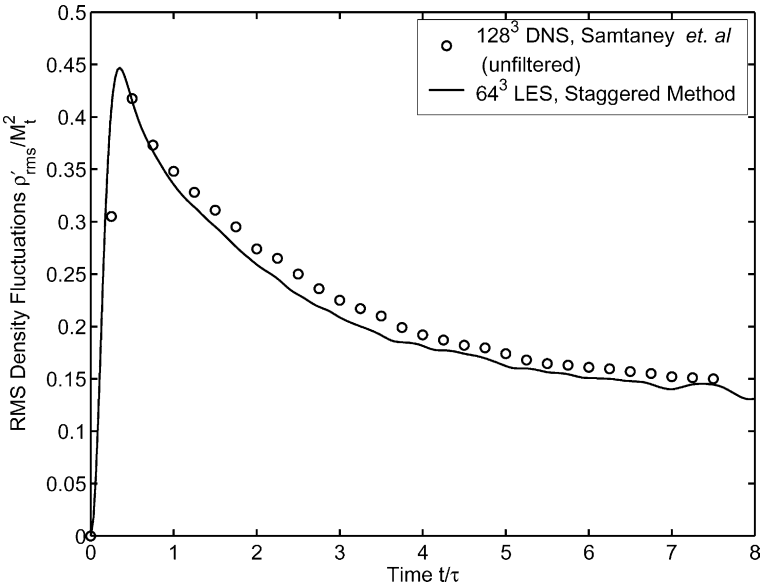

Fig. 18. Comparison of normalized density fluctuation evolution predicted by staggered LES with DNS of Samtaney et al. [23]. DNS results are unfiltered and time axis has been renormalized to match the definition of τ used herein.

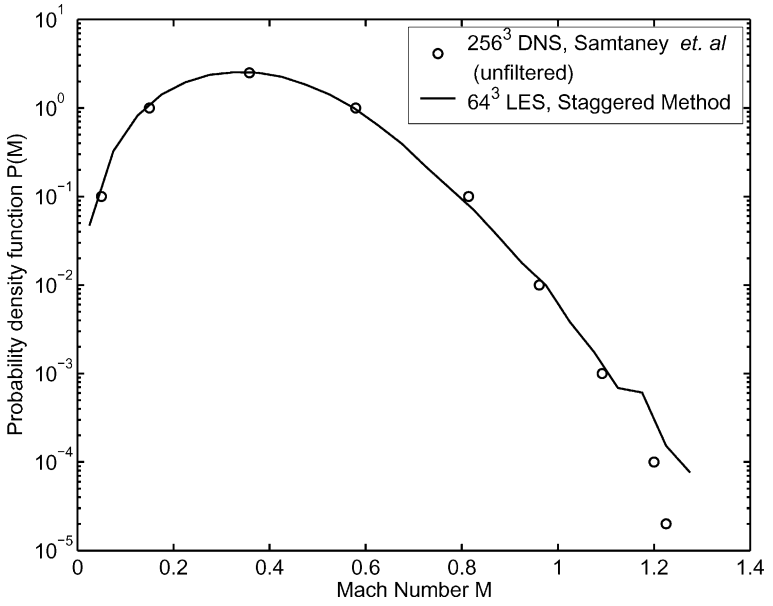

Fig. 19. Comparison of probability density function of Mach number from staggered LES (at $t/\tau = 1.95$) with DNS of Samtaney et al. [23] ($t/\tau = 1.56$ based on their units). DNS result is unfiltered.

well with DNS results except for low probability events at high Mach numbers where the PDF obtained herein shows statistical fluctuations due to the smaller number grid points available. Clearly, Mach number becomes locally supersonic, indicating the presence of eddy-shocklets as observed in [23] for this case.

7. Boundary schemes

Most problems of physical interest involve domains with non-periodic boundaries. To handle these, boundary schemes need to be introduced for differentiation and interpolation at the boundary and near boundary nodes. These schemes, by necessity, involve one sided differencing. Two properties need to be considered while developing these schemes: (1) order of accuracy should be as high as possible and (2) a discrete form of global conservation should be maintained. Boundary schemes satisfying these requirements have been derived for the staggered method and are presented in this section.

Consider the 1-D grid shown in Fig. 20 which shows the nodes and the numbering scheme at the left boundary. Clearly, two sets of boundary schemes are required, one for the ρ nodes and another for the ρu nodes.

7.1. Boundary schemes for the first derivative

A scheme for the first derivative at the boundary ρu-node ($j = 0$) may be written as

$$f'_0 + \hat{\alpha} f'_1 = \frac{1}{\Delta x}\left(a f_{1/2} + b f_{3/2} + c f_{5/2} + d f_{7/2}\right). \tag{32}$$

Third-order accuracy requires that the following relationships be satisfied:

$$\begin{aligned} a &= -\tfrac{1}{24}(23\hat{\alpha} + 71), \\ b &= \tfrac{1}{8}(7\hat{\alpha} + 47), \\ c &= \tfrac{1}{8}(\hat{\alpha} - 31), \\ d &= \tfrac{1}{24}(-\hat{\alpha} + 23), \end{aligned} \tag{33}$$

where $\hat{\alpha}$ is a free parameter and can be chosen to satisfy some constraint. For simplicity, we choose $\hat{\alpha} = 0$.

The interior scheme is not applicable at the ρu-node $j = 1$. Instead, the most compact fourth-order scheme obtained by setting $\hat{\alpha} = 1/22$ (which gives $b = 0$) in (13) is used. The scheme at $j = 2$ is also fourth-order accurate (given by (13)) and is obtained from a discrete conservation condition as described in Appendix B.

The first derivative at the boundary ρ-node ($j = 1/2$) may be obtained using a relation of the form

$$f'_{1/2} + \hat{\alpha} f'_{3/2} = \frac{1}{\Delta x}(a f_0 + b f_1 + c f_2 + d f_3). \tag{34}$$

Once again, a one-parameter family of third-order schemes is obtained with

$$\begin{aligned} a &= \tfrac{1}{24}(\hat{\alpha} - 23), \\ b &= \tfrac{1}{8}(-9\hat{\alpha} + 7), \\ c &= \tfrac{1}{8}(9\hat{\alpha} + 1), \\ d &= -\tfrac{1}{24}(\hat{\alpha} + 1). \end{aligned} \tag{35}$$

Discrete conservation requires that the point adjacent to the boundary ($j = 3/2$) use a scheme different from the interior scheme. The conservation condition and the boundary scheme that it yields are presented in Appendix B.

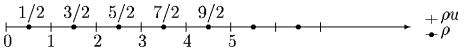

Fig. 20. Variable arrangement at left boundary in one dimension.

7.2. Boundary schemes for interpolation

A scheme for interpolating a function to the boundary ρu-node ($j = 0$) is

$$f_0^{\mathrm{I}} + \hat{\alpha} f_1^{\mathrm{I}} = a f_{1/2} + b f_{3/2} + c f_{5/2}. \tag{36}$$

Comparing coefficients of the Taylor expansion gives a third-order scheme with

$$\begin{aligned} a &= \tfrac{1}{8}(3\hat{\alpha} + 15), \\ b &= \tfrac{1}{4}(3\hat{\alpha} - 5), \\ c &= \tfrac{1}{8}(3 - \hat{\alpha}), \end{aligned} \tag{37}$$

where $\hat{\alpha}$ is chosen so that the coefficients a, b, and c are positive. This ensures that the interpolation process does not create any new extrema in the domain. However, such schemes were found to be unstable when integrated over long times. The scheme with $\hat{\alpha} = 0$ is stable and is used in the test cases presented herein. For the ρu-node $j = 1$, the most compact fourth-order interpolation scheme is used. This scheme is obtained by setting $b = 0$ and $\hat{\alpha} = 1/6$ in (19).

The interpolation scheme for the boundary ρ-node ($j = 1/2$) is written as

$$f_{1/2}^{\mathrm{I}} + \hat{\alpha} f_{3/2}^{\mathrm{I}} = a f_0 + b f_1 + c f_2 + d f_3. \tag{38}$$

This yields a fourth-order scheme with

$$\begin{aligned} a &= \tfrac{1}{16}(5 - \hat{\alpha}), \\ b &= \tfrac{1}{16}(9\hat{\alpha} + 15), \\ c &= \tfrac{1}{16}(9\hat{\alpha} - 5), \\ d &= \tfrac{1}{16}(1 - \hat{\alpha}), \end{aligned} \tag{39}$$

where $\hat{\alpha} = 0$ is chosen for simplicity. The interpolation scheme for the ρ-node $j = 3/2$ is chosen to be a fourth-order scheme given by (19). A value of $\hat{\alpha} = 0.25$ is used.

This is the complete set of boundary schemes required to extend the staggered method to non-periodic domains. In the following section, we test the performance of these schemes.

8. Evaluation of boundary schemes

Boundary schemes from the previous section are now applied to problems with inflow and outflow boundaries where non-reflecting boundary conditions based on the linearized Euler equations, as presented in [24], are used in their 1-D unsteady form. For details of implementation on the staggered mesh, see [25]. The boundary treatment has to satisfy the following requirements to be suitable for compressible flows: (a) reflection at the boundaries must be small and (b) should allow us to impose an incoming/outgoing turbulent stream. Model problems that test these characteristics are presented in this section.

First, we consider the reflection of a 1-D acoustic wave (generated by an initially Gaussian pressure distribution). Fig. 21 shows the time history of the L^2 norm (i.e., the root mean square) of the pressure fluctuation (from the uniform mean state). Four cases, with varying resolution (4, 8, 16, and 32 grid points across the initial pulse with fixed time step) are presented. The feature of interest is the sharp downward shift in the norm when the acoustic wave exits the boundary. The reflection coefficient, defined as the ratio of the norms after and before the wave exits the domain, varies from 1% to 0.1% when the pulse is well resolved. For ill-resolved pulses (4 and 8 points across the pulse), reflection is larger ($\sim$10%). It should be

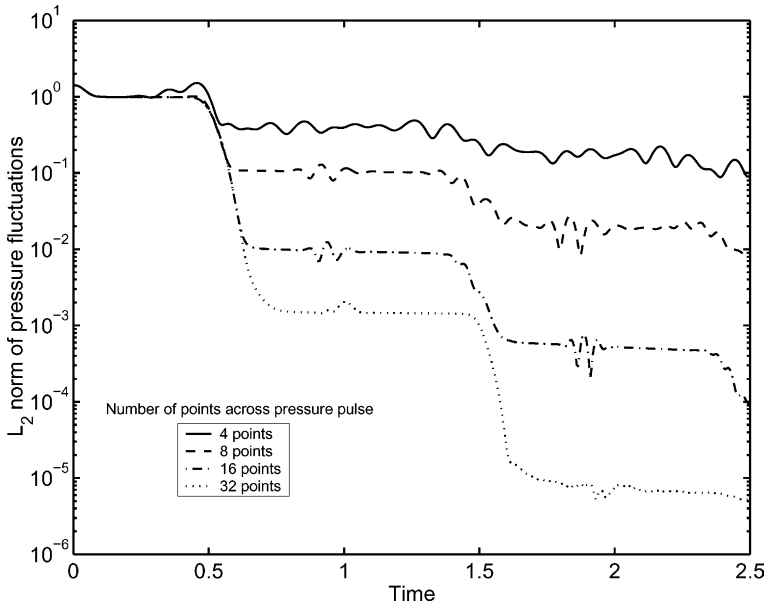

Fig. 21. Boundary scheme test – reflection of 1-D acoustic wave from inflow and outflow boundaries.

noted that after the first reflection, the waves that remain in the domain are ill-resolved, and subsequent reflection coefficients are therefore higher.

The second problem is that of reflection at the boundary of an acoustic wave generated by an initially Gaussian pressure distribution (in 2-D with 16 grid points across the pulse) of 5% amplitude is studied. The grid size used is 64×128. This generates a cylindrical pressure wave that interacts with the inflow/outflow boundary conditions in the x-direction (as shown in the contours of pressure fluctuations in Fig. 22). The domain in the x_2-direction is much larger than shown in the figure, so the reflections are from the x_1-boundaries alone. From Fig. 22, it is clear that reflection is very small (around 3% in terms of the maximum value of pressure fluctuations).

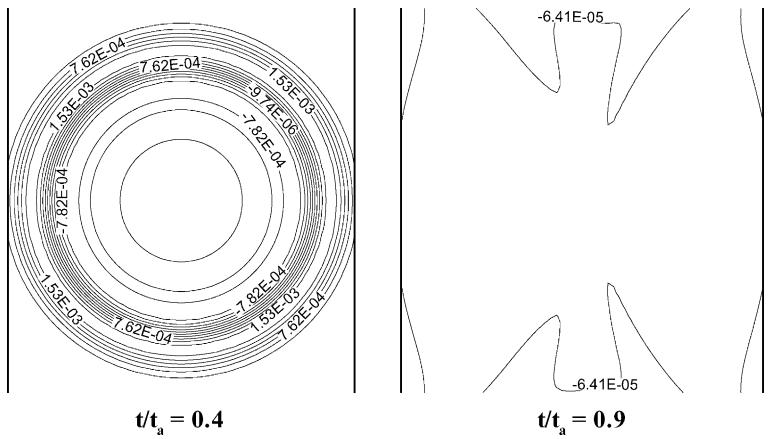

Fig. 22. Boundary scheme test – reflection of cylindrical wave from inflow and outflow boundaries.

Lastly, we assess the ability of our boundary treatment to pass large vortical structures. Tests with isolated vortices entering and leaving the domain have been carried out but the results are not presented here. Instead, we present the more complicated case of isotropic turbulence carried by a uniform mean stream of Mach number 0.25. At the inflow, the turbulent Mach number is 0.05, the Taylor microscale Reynolds number is about 500 and the velocity spectrum is given by (31). This simulation evaluates the ability to impose inflow turbulence as well as pass large vortical structures out of the domain. The decay of turbulent kinetic energy from the inflow to the outflow planes is compared to a temporal simulation in Fig. 23, where the spatial direction x_1 has been converted to a time variable using Taylor's hypothesis (i.e., $t = x/U_\infty$). There is some discrepancy at $t = 0$ which corresponds to the inflow plane. The lack of precise initial correspondence persists as a small difference between the two curves. Fig. 24 shows contours of instantaneous spanwise vorticity in a spanwise plane. The scales observed in the figure are to be expected as the initial field (at the inflow plane) develops smaller scales which are then dissipated by viscosity through the viscous and sub-grid terms.

The boundary schemes presented herein work well with characteristic boundary conditions developed by Giles [24]. Acoustic reflection at the boundaries is low, vortical structures exit the domain without significant reflection, and turbulence can be specified at the inflow plane.

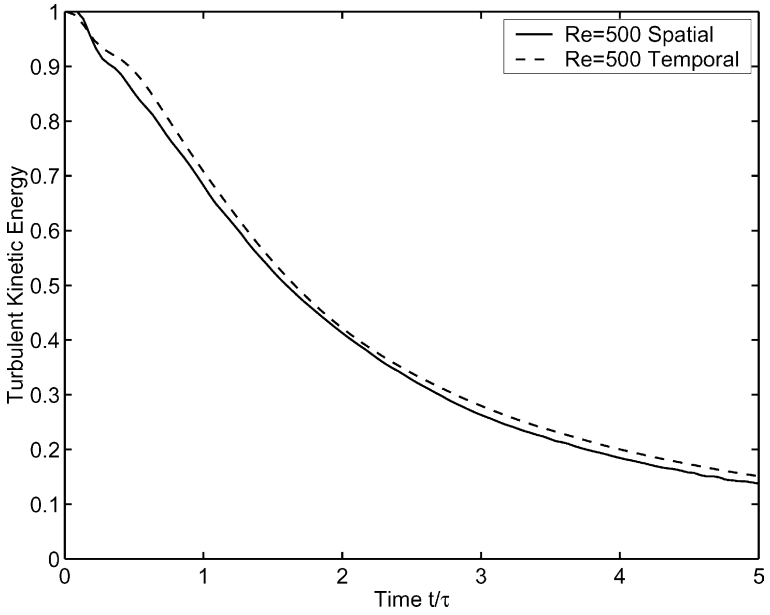

Fig. 23. Boundary scheme test – decay of turbulent kinetic energy predicted by simulation of spatially developing turbulence with inflow and outflow boundaries compared to a temporal simulation at same conditions.

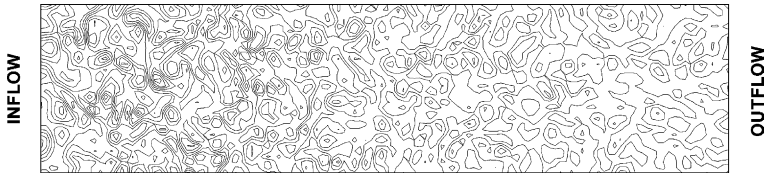

Fig. 24. Boundary scheme test – vorticity contours showing vortical structures entering and leaving the domain in a spatial simulation of decaying isotropic turbulence.

9. Conclusions

We have presented a new methodology for accurate large eddy simulation of compressible turbulent flows. The robustness of compact high-order schemes for LES has been improved by a staggered arrangement of variables. Staggering of the variables provides robustness at high Reynolds numbers while maintaining conservation and is therefore better suited for flows involving shocks. Robustness of the method has been illustrated through the test problem of decaying compressible isotropic turbulence. The staggered method provides significant improvement over collocated method I that uses the conservative form of the equations. Collocated method II also improves on collocated method I but suffers in terms of energy conservation. Staggering avoids this pitfall. Boundary schemes are also presented that allow application of this methodology to more general flows.

Acknowledgements

Support for Santhanam Nagarajan was provided by the Franklin P. Johnson Stanford Graduate Fellowship and the Center for Integrated Turbulence Simulations, as a part of ASCI.

Appendix A. Sub-grid model

In this section, the sub-grid terms in (9) are derived. Modeling terms in the momentum equation arise from filtering of non-linear (advective and diffusive) terms. The sub-grid contribution of the advection term is

$$\tau_{ij}^{\mathrm{sgs}} = \overline{\rho}\left(\widetilde{u_i u_j} - \widetilde{u}_i \widetilde{u}_j\right) \tag{A.1}$$

and needs to be modeled. The non-linearity in the viscous stress tensor σ_{ij} as defined in (3) leads to a sub-grid contribution

$$\overline{\sigma}_{ij} = \overline{\frac{\mu(\widetilde{T})}{Re}\left(2S_{ij} - \frac{2}{3}\delta_{ij}S_{kk}\right)} \tag{A.2}$$

$$= \frac{\mu(\widetilde{T})}{Re}\left(2\widetilde{S}_{ij} - \frac{2}{3}\delta_{ij}\widetilde{S}_{kk}\right) + \sigma_{ij}^{\mathrm{sgs}}, \tag{A.3}$$

where

$$S_{ij} = \frac{1}{2}\left(\frac{\partial u_i}{\partial x_j} + \frac{\partial u_j}{\partial x_i}\right), \tag{A.4}$$

$$\sigma_{ij}^{\mathrm{sgs}} = \overline{\frac{\mu(\widetilde{T})}{Re}\left(2S_{ij} - \frac{2}{3}\delta_{ij}S_{kk}\right)} - \frac{\mu(\widetilde{T})}{Re}\left(2\widetilde{S}_{ij} - \frac{2}{3}\delta_{ij}\widetilde{S}_{kk}\right). \tag{A.5}$$

The sub-grid term $\sigma_{ij}^{\mathrm{sgs}}$ is neglected [26].

Before the sub-grid terms in the energy equation are modeled, it needs to be noted that thermodynamic variables (pressure and temperature) are evaluated from conserved variables. Since these are related non-linearly, sub-grid terms arise. Specifically, pressure is related to the conserved variables by

$$\frac{p}{\gamma - 1} = E - \frac{1}{2}\rho u_k u_k. \tag{A.6}$$

Filtering this equation, we get

$$\frac{\overline{p}}{\gamma-1}=\overline{E}-\frac{1}{2}\overline{\rho}\widetilde{u}_k\widetilde{u}_k-\underbrace{\frac{1}{2}\overline{\rho}(\widetilde{u_k u_k}-\widetilde{u}_k\widetilde{u}_k)}_{\frac{1}{2}\tau_{kk}^{\mathrm{sgs}}}. \tag{A.7}$$

The term τ_{kk}^{sgs} appears in the momentum equation and is modeled in that context. It needs to be included in the definition for pressure as well.

The non-linear advection terms in the energy equation lead to a sub-grid term (q^k in (9)). This term is obtained as follows:

$$\begin{aligned}\overline{(E+p)u_j}&=\frac{\gamma}{\gamma-1}\overline{pu_j}+\frac{1}{2}\overline{\rho u_k u_k u_j}=\overline{\rho}\widetilde{Tu_j}+\frac{1}{2}\overline{\rho}\widetilde{u_k u_k u_j}\\&=\overline{\rho}\widetilde{T}\widetilde{u}_j+\overline{\rho}(\widetilde{Tu_j}-\widetilde{T}\widetilde{u}_j)+\frac{1}{2}\overline{\rho}\widetilde{u}_k\widetilde{u}_k\widetilde{u}_j+\frac{1}{2}\overline{\rho}\big(\widetilde{u_k u_k u_j}-\widetilde{u}_k\widetilde{u}_k\widetilde{u}_j\big).\end{aligned} \tag{A.8}$$

Using (A.7), this reduces to

$$\overline{(E+p)u_j}=\big(\overline{E}+\overline{p}\big)\widetilde{u}_j+\overline{\rho}(\widetilde{Tu_j}-\widetilde{T}\widetilde{u}_j)+\frac{1}{2}\overline{\rho}\big(\widetilde{u_k u_k u_j}-\widetilde{u_k u_k}\widetilde{u}_j\big). \tag{A.9}$$

Neglecting the last term on the right, we get a sub-grid heat flux (q_j^{sgs} in (9)) that has the form

$$q_j^{\mathrm{sgs}}=\overline{\rho}(\widetilde{Tu_j}-\widetilde{T}\widetilde{u}_j). \tag{A.10}$$

Modeling terms arising from the non-linearities in the heat flux term q_j and the work term $u_j\sigma_{jk}$ in the energy equation are neglected [26].

The sub-grid terms of (A.1) and (A.10) are modeled using the dynamic procedure of [13] with the modifications proposed by Lilly [27]. These are evaluated as follows:

$$\tau_{ij}^{\mathrm{sgs}}-\frac{1}{3}\tau_{kk}^{\mathrm{sgs}}\delta_{ij}=-2C\overline{\rho}\Delta^2|\widetilde{S}|\left(\widetilde{S}_{ij}-\frac{1}{3}\widetilde{S}_{kk}\delta_{ij}\right), \tag{A.11}$$

$$\tau_{kk}^{\mathrm{sgs}}=2C_I\overline{\rho}\Delta^2|\widetilde{S}|^2, \tag{A.12}$$

$$q_i^{\mathrm{sgs}}=-\frac{\overline{\rho}C\Delta^2|\widetilde{S}|}{Pr_{\mathrm{t}}}\frac{\partial\widetilde{T}}{\partial x_i}, \tag{A.13}$$

where C, C_I, and Pr_{t} are the sub-grid model coefficients that are evaluated using the dynamic procedure as

$$C=\frac{\big\langle\big(L_{ij}-\frac{1}{3}L_{kk}\delta_{ij}\big)M_{ij}\big\rangle}{\big\langle M_{pq}M_{pq}\big\rangle}, \tag{A.14}$$

$$C_I=\frac{\langle L_{kk}\rangle}{\big\langle 2\hat{\overline{\rho}}\hat{\Delta}^2|\hat{\widetilde{S}}|^2\big\rangle}, \tag{A.15}$$

$$Pr_{\mathrm{t}}=-C\frac{\langle N_iN_i\rangle}{\big\langle K_jN_j\big\rangle}, \tag{A.16}$$

where

$$L_{ij} = \widehat{\overline{\rho}\widetilde{u}_i\widetilde{u}_j} - \frac{1}{\hat{\overline{\rho}}}\widehat{\overline{\rho}\widetilde{u}_i}\widehat{\overline{\rho}\widetilde{u}_j}, \tag{A.17}$$

$$M_{ij} = -2\hat{\Delta}^2\hat{\overline{\rho}}|\hat{\widetilde{S}}|\left(\hat{\widetilde{S}}_{ij} - \frac{1}{3}\hat{\widetilde{S}}_{kk}\delta_{ij}\right) + 2\Delta^2\overline{\overline{\rho}|\widetilde{S}|\left(\widetilde{S}_{ij} - \frac{1}{3}\widetilde{S}_{kk}\delta_{ij}\right)}, \tag{A.18}$$

$$N_i = \hat{\Delta}^2\hat{\overline{\rho}}|\hat{\widetilde{S}}|\frac{\partial\hat{\widetilde{T}}}{\partial x_i} - \overline{\Delta^2\overline{\rho}|\widetilde{S}|\frac{\partial\widetilde{T}}{\partial x_i}}, \tag{A.19}$$

$$K_i = \widehat{\overline{\rho}\widetilde{u}_i\widetilde{T}} - \frac{1}{\hat{\overline{\rho}}}\widehat{\overline{\rho}\widetilde{u}_i}\widehat{\overline{\rho}\widetilde{T}}. \tag{A.20}$$

In these equations, the angular brackets $\langle\cdot\rangle$ denote averaging along homogeneous directions (volume average in case of homogeneous isotropic turbulence) and the hat $\hat{\cdot}$ represents a test filter which is chosen to be the explicit seven point least-squares filter defined in [18] as

$$\hat{f}_j = 0.5f_j + 0.6744132\frac{f_{j-1} + f_{j+1}}{2} - 0.1744132\frac{f_{j-3} + f_{j+3}}{2} \tag{A.21}$$

and is applied successively in all three directions.

In the staggered method, all sub-grid model coefficients are calculated at the ρ-node by evaluating L_{ij}, M_{ij}, N_i, and K_i at this node. The model coefficients are then interpolated to the nodes (corresponding to viscous stresses τ_{ij} and heat flux q_i) where they are needed for evaluation of the sub-grid stress tensor τ_{ij}^{sgs} and heat flux vector q_i^{sgs}, respectively.

Appendix B. Discrete conservation

Boundary schemes are selected to satisfy a discrete form of global conservation which ensures conservation for linear equations with constant coefficients. This does not translate into discrete conservation for non-linear equations involving the interpolation operation.

The staggered compact scheme may be written in matrix form as

$$\mathbf{A}\mathbf{f}' = \frac{1}{\Delta x}\mathbf{B}\mathbf{f}, \tag{B.1}$$

where $\mathbf{A}$ is an $N \times N$ tridiagonal matrix, $\mathbf{B}$ is an $N \times N$ matrix with four diagonals, $\mathbf{f}$ is an N-vector consisting of the function values at the nodes, and $\mathbf{f}'$ is the N-vector of derivatives located $\Delta x/2$ away from $\mathbf{f}$. To satisfy the global conservation constraint, it is required that all the columns of the matrix $\mathbf{B}$, except the first and last ones, add up to zero (see [8]). This ensures that only the boundary fluxes contribute to the change inside the domain and thus enforces global conservation.

The discrete conservation condition needs to be applied to both sets of boundary schemes described earlier. Evaluation of derivatives at the ρu-nodes (see Fig. 20) lead to a **B** matrix as shown below

$$\mathbf{B} = \begin{bmatrix} w_0a_0 & w_0b_0 & w_0c_0 & w_0d_0 & 0 & \cdots \\ -w_1a_1 & w_1a_1 & 0 & 0 & 0 & \cdots \\ -w_2b_2/3 & -w_2a_2 & w_2a_2 & w_2b_2/3 & 0 & \cdots \\ 0 & -b/3 & -a & a & b/3 & \cdots \\ 0 & 0 & -b/3 & -a & a & \cdots \\ 0 & 0 & 0 & -b/3 & -a & \cdots \\ 0 & 0 & 0 & 0 & -b/3 & \cdots \\ \vdots & \vdots & \vdots & \vdots & \vdots & \ddots \end{bmatrix}, \tag{B.2}$$

where the coefficients $\{a_0, b_0, c_0, d_0\}$ in the first row correspond to the boundary scheme given by (32) and are evaluated by choosing a value for $\hat{\alpha}$ in (32) ($\hat{\alpha} = 0$ is selected in this case). The coefficient a_1 in the second row corresponds to the most compact fourth-order scheme obtained by setting $\hat{\alpha} = 1/22$ in (13) and the coefficients a_2, b_2 in the third row correspond to a fourth-order scheme (to be chosen to satisfy conservation) given by (13). The weights w_0, w_1, w_2 are also to be chosen so as to satisfy global conservation. The coefficients a, b correspond to the interior difference scheme obtained by setting $\hat{\alpha} = 9/62$ in (13). The conservation condition requires that all columns except the first and last ones sum to zero

$$\begin{aligned} &w_0b_0 + w_1a_1 - w_2a_2 = \frac{b}{3}, \\ &w_0c_0 + w_2a_2 = a + \frac{b}{3}, \\ &w_0d_0 + \frac{1}{3}w_2b_2 = \frac{b}{3}. \end{aligned} \tag{B.3}$$

These are three equation in four unknowns w_0, w_1, w_2, and $\hat{\alpha}$ (corresponding to a_2 and b_2). Therefore we have one free parameter, which we choose as w_2 without loss of generality. It has been observed that certain values of w_2 lead to boundary schemes that are unstable. The value $w_2 = 1.1$ is found to be stable and is used. The value of $\hat{\alpha}$ obtained with $w_2 = 1.1$ is used to provide the difference scheme for the point $j = 2$. This set now satisfies the global conservation condition.

A similar analysis is required for evaluation of derivatives at the ρ-nodes (Fig. 20). The right-hand side matrix **B** is

$$\mathbf{B} = \begin{bmatrix} w_0a_0 & w_0b_0 & w_0c_0 & w_0d_0 & 0 & \cdots \\ -w_1b_1/3 & -w_1a_1 & w_1a_1 & w_1b_1/3 & 0 & \cdots \\ 0 & -b/3 & -a & a & b/3 & \cdots \\ 0 & 0 & -b/3 & -a & a & \cdots \\ 0 & 0 & 0 & -b/3 & -a & \cdots \\ 0 & 0 & 0 & 0 & -b/3 & \cdots \\ \vdots & \vdots & \vdots & \vdots & \vdots & \ddots \end{bmatrix}, \tag{B.4}$$

where the coefficients $\{a_0, b_0, c_0, d_0\}$ in the first row correspond to the boundary scheme given by (34). $\hat{\alpha} = 0$ is chosen for this case. The coefficients $\{a_1, b_1\}$ in the second row correspond to a fourth-order scheme which is to be chosen so that the conservation condition is satisfied. Once again, w_0 and w_1 are weights that need to be obtained using the conservation condition. The conservation requirement yields

$$\begin{aligned} w_0 b_0 - w_1 a_1 &= \frac{b}{3}, \\ w_0 c_0 + w_1 a_1 &= a + \frac{b}{3}, \\ w_0 d_0 + \frac{1}{3} w_1 b_1 &= \frac{b}{3}. \end{aligned} \tag{B.5}$$

These are three equations in three unknowns (a_1 and b_1 are uniquely determined by the parameter $\hat{\alpha}$ through Eqs. (14) and (15)) and can be solved to give

$$w_0 = \frac{223}{186}, \quad w_2 = \frac{61}{62}, \quad \hat{\alpha} = \frac{37}{183}. \tag{B.6}$$

References

[1] A. Pascarelli, U. Piomelli, G.V. Candler, Multi-block large-eddy simulations of turbulent boundary layers, J. Comput. Phys. 157 (2000) 256.
[2] D.P. Rizzetta, M.R. Visbal, D.V. Gaitonde, Large-eddy simulation of supersonic compression-ramp flow by high-order method, AIAA J. 39 (2001) 2283.
[3] H. Yan, D. Knight, Large-eddy simulation of supersonic flat plate boundary layer part i, AIAA Paper 2002-0132.
[4] K. Akselvoll, P. Moin, Large-eddy simulation of turbulent confined coannular jets, J. Fluid Mech. 315 (1996) 387.
[5] C.D. Pierce, Progress-variable approach for large eddy simulation of turbulent combustion, Ph.D. thesis, Stanford University, 2001.
[6] Y. Morinishi, T.S. Lund, O.V. Vasilyev, P. Moin, Fully conservative higher order finite difference schemes for incompressible flow, J. Comput. Phys. 143 (1998) 90.
[7] S. Ghosal, An analysis of numerical errors in large eddy simulation of turbulence, J. Comput. Phys. 125 (1998) 187.
[8] S.K. Lele, Compact finite difference schemes with spectral-like resolution, J. Comput. Phys. 103 (1992) 16.
[9] S.S. Lee, S.K. Lele, P. Moin, Interaction of isotropic turbulence with shock waves: effect of shock strength, J. Fluid Mech. 340 (1997) 225.
[10] K. Mahesh, S.K. Lele, P. Moin, The influence of entropy fluctuations on the interaction of turbulence with a shock wave, J. Fluid Mech. 334 (1997) 353.
[11] T. Freund, S.K. Lele, P. Moin, Compressibility effects in a turbulent annular mixing layer, part 1. Turbulence and growth rate, J. Fluid Mech. 421 (2000) 229.
[12] T. Colonius, S.K. Lele, P. Moin, Sound generation in a mixing layer, J. Fluid Mech. 330 (1997) 375.
[13] P. Moin, K. Squires, W. Cabot, S. Lee, A dynamic subgrid-scale model for compressible turbulence and scalar transport, Phys. Fluids A 3 (1991) 2746.
[14] A. Honein, personal communication.
[15] G.S. Constantinescu, S.K. Lele, Large eddy simulation of a near sonic turbulent jet and its radiated noise, AIAA Paper 2001-0376.
[16] G.A. Blaisdell, Numerical simulations of compressible homogeneous turbulence, Ph.D. thesis, Stanford University, 1991.
[17] G.A. Blaisdell, E.T. Spyropoulos, J.H. Qin, The effect of the formulation of nonlinear terms on aliasing errors in spectral methods, Appl. Numer. Math. 21 (1996) 207.
[18] E.T. Spyropoulos, G.A. Blaisdell, Evaluation of the dynamic model for simulations of compressible decaying isotropic turbulence, AIAA J. 34 (1996) 990.
[19] D.A. Kopriva, A staggered-grid multidomain spectral method for the compressible Navier–Stokes equations, J. Comput. Phys. 143 (1998) 125.
[20] G.S. Djambazov, C.-H. Lai, K.A. Pericleous, Staggered-mesh computation for aerodynamic sound, AIAA J. 38 (2000) 16.
[21] F.H. Harlow, J.E. Welch, Numerical calculation of time dependent viscous incompressible flow of fluid with a free surface, Phys. Fluids 8 (1965) 2182.
[22] G. Comte-Bellot, S. Corrsin, Simple Eulerian time correlations of full- and narrow-band velocity signals in grid-generated isotropic turbulence, J. Fluid Mech. 48 (1971) 273.
[23] R. Samtaney, D.I. Pullin, B. Kosovic, Direct numerical simulation of decaying compressible turbulence and shocklet statistics, Phys. Fluids 13 (2001) 1415.

[24] M.B. Giles, Nonreflecting boundary conditions for Euler equation calculations, AIAA J. 28 (1990) 2050.
[25] S. Nagarajan, Ph.D. thesis, Stanford University (in preparation).
[26] B. Vreman, B. Geurts, H. Kuerten, Subgrid-modeling in LES of compressible flow, Appl. Sci. Res. 54 (1995) 191.
[27] D.K. Lilly, A proposed modification of the Germano subgrid-scale closure method, Phys. Fluids A 4 (1992) 633.